PCCP

PAPER

View Article Online
View Journal | View Issue

Cite this: *Phys. Chem. Chem. Phys.*, 2015, **17**, 31145

Spatiotemporal dynamics of solvent-assisted lipid bilayer formation†

Min Chul Kim,[ab] Jurriaan J. J. Gillissen,[ab] Seyed R. Tabaei,[ab] Vladimir P. Zhdanov[abc] and Nam-Joon Cho*[abd]

Received 4th October 2015,
Accepted 28th October 2015

DOI: 10.1039/c5cp05950j

www.rsc.org/pccp

The solvent-assisted lipid bilayer (SALB) method offers a general strategy to fabricate supported lipid bilayers on solid surfaces. In this method, lipids dissolved in alcohol are deposited on the target substrate in parallel with their aggregation during exchange with aqueous buffer solution which promotes spontaneous bilayer formation. Herein, a combination of experimental and theoretical approaches is employed in order to understand the key aspects of the SALB formation process. Epifluorescence microscopy experiments are conducted in order to measure the spatiotemporal dynamics of bilayer formation on a glass substrate in a microfluidic channel. Corresponding snapshots of bilayer formation at different stages are rationalized by a numerical simulation of solvent displacement inside the channel. Comparing simulation with experiment indicates that in close proximity to the side walls of the present setup, the bilayer formation is confined to a relatively thin region behind the moving solvent displacement front.

Introduction

Phospholipid assemblies on solid supports have widely been utilized as a representative biomimetic platform, providing a model to study the complex nature of cellular membranes for fundamental knowledge as well as various applications such as medical diagnostics and drug discovery.[1–4] A supported lipid bilayer is one of the best examples of a biomimetic membrane. The physical and chemical properties of such membranes on solid supports have been characterized by various surface-sensitive techniques, including a quartz crystal microbalance with dissipation (QCM-D) monitoring,[5] epifluorescence microscopy[6], atomic force microscopy,[7] fluorescence recovery after photobleaching (FRAP)[8,9] and localized surface plasmon resonance.[10]

Among various methods of fabrication of supported lipid bilayers, the vesicle fusion method is one of the most convenient.[11,12] It involves vesicle adsorption and rupture after the vesicles reach a critical coverage on hydrophilic substrates such as silicon oxide,[3] glass,[5,6] or mica.[13] The corresponding governing parameters include lipid composition,[14] vesicle size,[15] vesicle lamellarity,[16] solution pH,[17] temperature,[18] ionic strength[19] and osmotic pressure.[12,20] Vesicle rupture limits the applicability of the vesicle fusion method to sufficiently small, fluid-phase lipid vesicles and poses additional constraints on the properties of the supporting solid surface.

To overcome the limits of the vesicle fusion procedure and extend the applicability of supported lipid bilayers, an alternative procedure for fabricating supported lipid bilayers has recently been developed and is referred to as the solvent-assisted lipid bilayer (SALB) method. This method is partly based on earlier observations,[21] involving the exchange of an organic solvent, containing lipids in either monomer or inverted cylindrical micelle form, to an aqueous solution (water or buffer). This exchange induces a sequence of transitions of the lipid phase from inverted micelles and monomers, to conventional micelles and vesicles. In a relatively late stage of the solvent exchange, *i.e.*, at an appreciable water content, the phase transition to micelles and vesicles is believed to induce the formation of a complete supported lipid bilayer on the inside wall of the lipid solution containing vessel. The process of solvent replacement and subsequent bilayer formation can be realized, by flowing water through a channel that is initially filled with lipids dissolved in an organic solvent. As the water mixes with the lipid solution, the lipid solvent is gradually exchanged from organic to water, leading to the formation of a lipid bilayer on the channel wall.[22] As compared to the vesicle fusion method the SALB method does not require vesicle preparation and is applicable to a wider variety of solid

[a] *School of Materials Science and Engineering, Nanyang Technological University, 50 Nanyang Avenue 639798, Singapore. E-mail: njcho@ntu.edu.sg*
[b] *Centre for Biomimetic Sensor Science, Nanyang Technological University, 50 Nanyang Drive 637553, Singapore*
[c] *Boreskov Institute of Catalysis, Russian Academy of Sciences, Novosibirsk 630090, Russia*
[d] *School of Chemical and Biomedical Engineering, Nanyang Technological University, 62 Nanyang Drive 637459, Singapore*

† Electronic supplementary information (ESI) available. See DOI: 10.1039/c5cp05950j

supports[22,23] and lipid compositions,[24] enabling the formation of gel-phase supported lipid bilayers among other possibilities.

While previous SALB studies mainly focus on temporal kinetics[22,25] and bilayer properties after complete solvent exchange[22–26], the spatiotemporal dynamics of the SALB formation have not yet been extensively studied. Focusing on the latter aspects, we report herein the first results of our observation of the microscopic dynamics of the SALB formation of fluorescently labeled lipids on a glass substrate in a microfluidic channel. In order to better interpret the observations, we numerically simulate the solvent exchange in the channel and present a detailed analysis of the transient diffusion of components of mixed solution in the sensor channel under flow conditions. While there are various reported treatments of the role of diffusion in biosensors operating under no-flow conditions (see, *e.g.*, ref. 27), treatments focused on flow conditions are still rare and our study provides a comprehensive analysis of this aspect in relation to the SALB formation process.

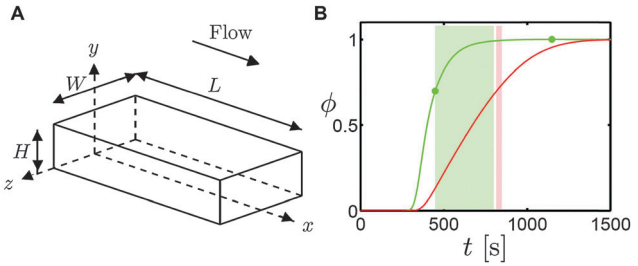

Fig. 1 Schematic representation of the epifluorescence microscopy experiments. (A) The microfluidic channel has a length of L = 48 mm (x-direction), a width of W = 5 mm (z-direction) and a height of H = 0.1 mm (y-direction). The channel inlet and outlet correspond to x = 0 and x = L, the bottom and top walls correspond to y = 0 and y = H and the channel side walls correspond to $z = -W/2$ and $z = W/2$, respectively. (B) The simulated solvent exchange from pure isopropanol (ϕ = 0) to pure water (ϕ = 1) as a function of time t in the center of the bottom channel wall at $x = L/2$, y = 0 and z = 0 (green line) and on the bottom close to the channel side at $x = L/2$, y = 0 and $z = W/2$ (red line). The epifluorescence image sequence time intervals at the center (Fig. 2) and close to the side (Fig. 3A) are indicated by the areas shaded in green and red, respectively. The FRAP measurements (Fig. 4) are conducted at the time instances, indicated by the green, circular markers.

Materials and methods

Lipid sample preparation

The selected lipid composition for the SALB experiments was 99.9 mol% zwitterionic 1,2-dioleoyl-*sn-glycero*-3-phosphocholine, referred to as DOPC (Avanti Polar Lipids, Alabaster, AL, USA), and 0.1 mol% fluorescently labeled 1,2-dioleoyl-*sn-glycero*-3-phosphoethanolamine-*N*-(lissamine rhodamine B sulfonyl) (ammonium salt), referred to as the Rh-PE fluorophore. The lipid in powder stock was dissolved in isopropanol at a concentration of 0.5 mg mL^{-1} (equivalent to μg mm^{-3} units), which was previously reported to be the most effective concentration for SALB formation.[26] An aqueous buffer solution of 150 mM NaCl and 10 mM Tris [pH 7.5] was employed for the solvent-exchange step. All the buffer solutions are prepared with 18.2 MΩ cm MilliQ-treated water (Millipore, Billerica, MA).

Epifluorescence microscopy experiments

Epifluorescence microscopy was employed to observe the spatiotemporal dynamics of SALB formation on the glass bottom of a rectangular microfluidic channel, with a width to height ratio of 50 (sticky-Slide I 0.1 Luer, Ibidi, Germany). The channel has a length of L = 48 mm (x-direction), a width of W = 5 mm (z-direction) and a height of H = 0.1 mm (y-direction) (Fig. 1A). The channel inlet and outlet correspond to x = 0 and x = L, the bottom and top walls correspond to y = 0 and y = H, and the channel side walls correspond to $z = -W/2$ and $z = W/2$, respectively. The channel is initially filled with DOPC lipids dissolved in isopropanol. The channel is connected to a reservoir containing the aqueous buffer solution *via* one series of four circular cross-sectional tubes of slightly different diameters (the goal of their use is mixing the buffer with the lipid isopropanol solution). Details of the tubes are provided in Table S1 in the ESI.† The outlet of the channel is connected to a pump. At t = 0 the pump starts driving the buffer from the reservoir through the tubes and the channel, at a volumetric flow rate of Q = 0.68 mm^3 s^{-1}, which corresponds to a cross-sectional averaged fluid velocity in the channel of $U = Q/(WH)$ = 1.36 mm s^{-1}.

The buffer takes a time of $\tau = V/Q$ = 600 s to pass through the tubes, where $V = \sum_{i=1}^{4} \pi R_i^2 L_i$ is their total volume, R_i is radius of the ith tube and L_i is the length of the ith tube. Similarly we compute a time of 36 s required for the buffer to pass through the channel, which is small compared to the tubing passage time. During the 600 s passage time, the buffer mixes with the lipid isopropanol solution inside the tubes. The mixing is due to the combined effect of advection and diffusion, referred often to as a Taylor Aris dispersion.[28] As an effect of the Taylor Aris dispersion, there is a smooth temporal transition of the solvent composition exiting the tubes into the channel. Below, we numerically compute the time scale of this transition to be τ_t = 600 s. This means that the stepwise solvent exchange from isopropanol to water, which is imposed at t = 0 at the tubing inlet, is transformed by the action of advection and diffusion into a smooth transition, ranging between $\tau - \tau_t/2$ = 300 s and $\tau + \tau_t/2$ = 900 s at the channel inlet.

During the solvent exchange, epifluorescence microscopy images are taken using an inverted optical microscope (Eclipse TI-U microscope; Nikon, Japan) with a 60× magnification (NA = 1.49) oil immersion objective lens (Nikon) and an iXon 512 × 512 pixel EMCCD camera (Andor Technology, Northern Ireland), resulting in a square image of 137 μm × 137 μm with a pixel size of 0.267 μm × 0.267 μm. The sample was illuminated with a fiber-coupled mercury lamp (Intensilight C-HGFIE; Nikon) and a TRITC filter was used to filter the excitation light from the emission light by the Rh-PE fluorophores.

Fluorescence recovery after photobleaching (FRAP) measurements

Fluorescence recovery after photobleaching (FRAP) measurements were performed in order to determine lateral lipid fluidity of

supported lipid bilayers formed by the SALB method. For this purpose a circular bilayer spot of 20 μm diameter is photobleached for five seconds with a 532 nm, 100 mW laser beam. The recovery of the fluorescence intensity within the spot is measured during the following minute at one second intervals. The corresponding diffusion coefficients are calculated based on the Hankel transform method.[9]

Results

SALB experiments

Epifluorescence microscopy images are taken to observe the spatiotemporal dynamics of SALB formation on the bottom glass wall of the microfluidic channel at two different locations. The first location is at the center of the bottom wall, *i.e.*, at $x = L/2$, $y = 0$ and $z = 0$. The green line in Fig. 1B shows the computed solvent exchange as a function of time at this location (for the details of calculations, see discussion below). The line shows a smooth transition from pure isopropanol ($\phi = 0$) at $t = 300$ s to pure buffer ($\phi = 1$) at $t = 900$ s. The second location is close to the channel side, *i.e.*, at $x = L/2$, $y = 0$ and $z = W/2$. The corresponding solvent exchange (Fig. 1B, red line) is delayed compared to that at the channel center, with a transition from isopropanol to buffer between $t = 300$ s and $t = 1500$ s. The delay is related to the cross-stream velocity distribution in both the tubes as well as in the channel. The details of the cross-stream, solvent exchange distribution are studied numerically below.

Lipid bilayer spreading. Fig. 2 shows four consecutive snapshots of the fluorescence intensity in the center of the bottom channel wall, *i.e.* at $x = L/2$, $y = 0$ and $z = 0$. The snapshots cover the period between $t = 450$ s and $t = 800$ s (Fig. 1B, green shaded area). During the exchange from the organic to aqueous solvent in the channel, one observes the appearance of lipid patches on the surface. With subsequent merger of these patches, a complete lipid bilayer forms (see Video S1 in the ESI† for a full-length movie of Fig. 2). Apart from the random fluctuations, no spatial gradients are observed in the fluorescence intensity in Fig. 2. This means that the bilayer formation is uniform on the scale of the image, *i.e.*, 100 μm. More intricate formation patterns are observed (Fig. 3A) close to the channel side walls, *i.e.*, at $x = L/2$, $y = 0$ and $z = W/2$. The nine snapshots in Fig. 3A cover the period between $t = 820$ s and $t = 850$ s (see Fig. 1B, red shaded area). Here one can observe a sharp front, separating the fully formed bilayer from the region, where the bilayer is not yet fully formed (see Video S2 in the ESI† for a full-length movie of Fig. 3A).

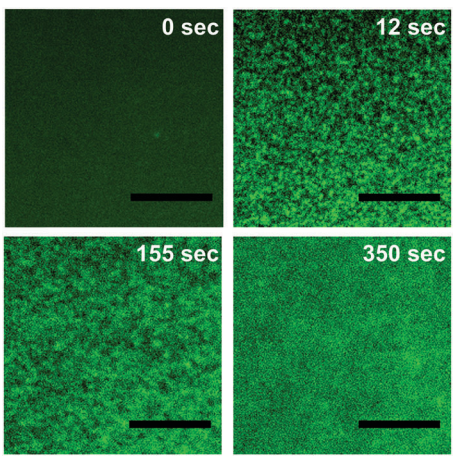

Fig. 2 Observations of supported lipid bilayer formation in the channel center. Fluorescence micrographs are 53 μm and 53 μm in the horizontal (x) and vertical (z) direction. The scale bars represent 20 μm. The times indicated in the panels are relative to the first image, which was taken roughly 450 s after starting the pump.

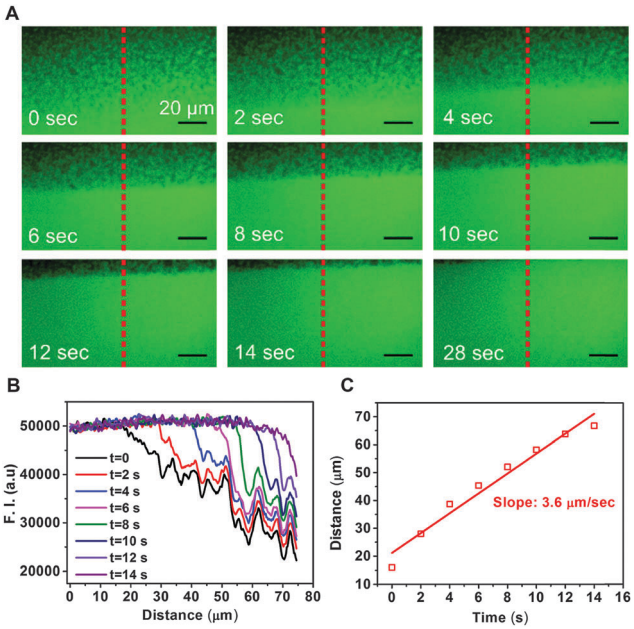

Fig. 3 Observation of supported lipid bilayer formation at the channel side. (A) Fluorescence micrographs of SALB formation taken at $x = L/2$, $y = 0$ and $z = W/2$. The image dimensions in the horizontal (x) and vertical (z) directions are 137 μm and 75 μm, respectively. The scale bars represent 20 μm. The distance from the image center to the channel side wall is estimated as 170 ± 70 μm. The times indicated in the panels are relative to the first image, which was taken roughly 800 s after starting the pump. (B) Fluorescence intensity along the dashed lines specified in (A). (C) Time-dependent bilayer front position, which is defined as the position where the fluorescence intensity in (B) starts to decline.

Fig. 3B shows the fluorescence intensity I as a function of the span-wise coordinate z at various time instances t. These profiles are obtained along the dashed lines that are shown in Fig. 3A. Below a certain position, which we call the lipid bilayer front position z_L, the intensity profiles $I(z)$ are observed to be rather constant, apart from random fluctuations, while above this position the profiles are observed to decline. The constant part reflects the fully developed lipid bilayer, while the declining part reflects the region where the bilayer is under development. As time progresses the intensity profiles are observed to move towards the wall, which corresponds to an increasing lipid bilayer front position z_L. From the data in Fig. 3B we determine by eye the values for z_L at the various time instances. By plotting z_L as a function of t in Fig. 3C, the bilayer formation velocity is determined to be 3.6 μm s^{-1}.

Lipid bilayer fluidity. Fluorescence recovery after photobleaching (FRAP) measurements are performed in order to determine the lateral lipid fluidity of the forming supported lipid bilayer. Measurements are taken in the center of the bottom channel wall, *i.e.*, at $x = L/2$, $y = 0$, and $z = 0$. Two FRAP experiments are conducted at two different times, $t = 450$ s and $t = 1150$ s (Fig. 1B, green circular markers), corresponding to incomplete and complete stages of the solvent exchange process. After incomplete solvent exchange (Fig. 4A and C), there is an incomplete recovery of the fluorescence intensity in the bleached region throughout the post-bleaching period. This indicates that the bilayer is not completely formed yet, *i.e.*, the lipid patches are disconnected and the lipid diffusion is nearly negligible. By contrast, after full solvent exchange (Fig. 4B and D), there is a nearly complete recovery of the fluorescence intensity after photobleaching. For this case the Hankel transform method[9] yields a lateral diffusion coefficient of 2.3 ± 0.2 μm^2 s^{-1}. This value agrees well with the reference value of 2.5 μm^2 s^{-1} for supported lipid bilayers.[9] This agreement confirms that the supported lipid bilayer is completely formed after full solvent exchange.

Simulation of solvent-exchange

To interpret the experimental observations displayed in Fig. 3, one should describe lipid adsorption and micelle and vesicle adsorption and rupture occurring in parallel with phase transitions in solution under transient flow conditions. Due to the complex physics of phase transitions (with many uncertain details) and hydrodynamics, the accurate full-scale solution of this problem is impossible. In our present treatment, we focus on the hydrodynamical aspects of the problem, *i.e.*, on the solvent exchange itself. Taking into account that the fraction of lipid in solution is low, we scrutinize the water–isopropanol exchange. The analysis of this part of the problem is mandatory for the understanding of the entire SALB formation process. Our experience indicates (see below) that this analysis alone makes it possible to rationalize the front propagation shown in Fig. 3.

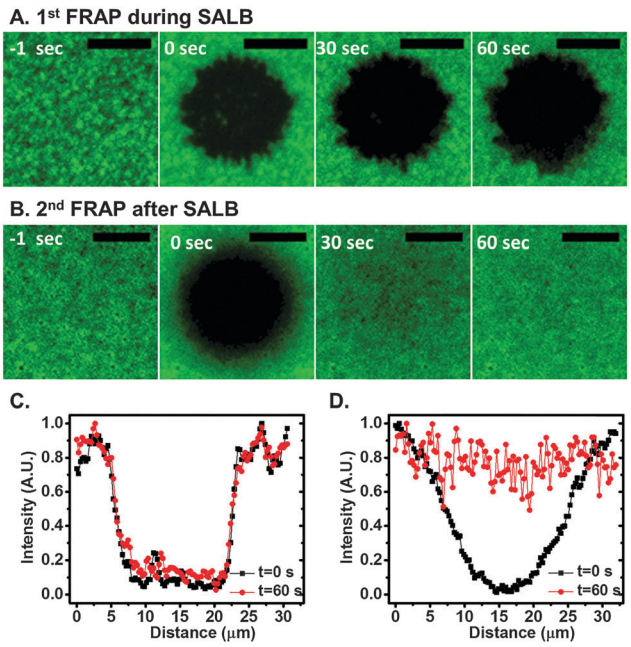

Fig. 4 Fluorescence recovery after photobleaching (FRAP) measurements. FRAP measurements at (A and C) incomplete solvent exchange and (B and D) complete solvent exchange taken at the center of the bottom channel wall, *i.e.* at $x = L/2$, $y = 0$ and $z = 0$. Fluorescence intensity as a function of x (horizontal) and z (vertical) coordinates (A and B) and as a function of x (C and D). The scale bars in A and B represent 10 μm. The times indicated in the panels in A are relative to the moment of photobleaching. They are not related to the times indicated in the panels of Fig. 3A.

The hydrodynamics of solvent exchange depend on the viscosity and diffusion coefficients characterizing the water–isopropanol mixture. Both these coefficients depend on the water fraction in solution. An additional complicating factor is that the water–isopropanol exchange profiles in the channel depend on those in the four feed tubes (as detailed in Table S1 in the ESI†). The radii of these tubes are different and the circular cross section of the fourth tube near the inlet to the channel does not perfectly fit the width of the channel. The boundary conditions near the tube–tube and tube–channel contacts cannot be formulated very accurately. Bearing this in mind, we simplify our analysis by using the constant effective viscosity and diffusion coefficients, ν and D. In the water–isopropanol mixture, D varies as a function of ϕ in the range from 2×10^{-4} mm^2 s^{-1} to 1.2×10^{-3} mm^2 s^{-1}.[29] In this work, we use the value $D = 5 \times 10^{-4}$ mm^2 s^{-1}.

For a general qualitative introduction into the analysis, it is instructive to give a few simple estimates related to the evolution of the solvent in the channel. As mentioned above, due to the combined effect of advection and diffusion in the feeding tubes, the solvent at the channel inlet smoothly changes from pure isopropanol at $t = 300$ s to pure buffer at $t = 900$ s, *i.e.*, during the transition time of 600 s. The solvent passes through the channel in a relatively short time of 36 s. This short time implies that the solvent in the channel is uniformly distributed over the stream-wise (x) direction. In the cross-stream directions (y and z), the situation is more complex. To characterize the cross-stream non-uniformities, we estimate the cross-stream diffusion penetration depth $\delta = \sqrt{4Dt}$, where $t = x/U$ is the time for the solvent to travel from the channel inlet to the measurement region, which is halfway in the channel ($x = L/2$). Using $D = 5 \times 10^{-4}$ mm^2 s^{-1},[29] $L = 48$ mm, and $U = 1.4$ mm s^{-1}, we obtain a penetration depth of $\delta = 0.2$ mm. Since δ is larger than the channel height $H = 0.1$ mm, the solvent distribution is expected to be uniform over the wall-normal coordinate y. In contrast, the channel width $W = 5$ mm is appreciably larger than δ. This suggests a non-uniform solvent distribution over the span-wise coordinate z, which is numerically confirmed below as seen by a uniform solvent distribution over x and y and a non-uniform distribution over z.

The cross-stream penetration depth δ above can be interpreted as the thickness of the cross-stream solvent displacement front, which separates the region of pure isopropanol from that of pure buffer. If the propagation of the displacement front

is driven purely by diffusion, we can estimate its propagation speed as $\sqrt{D/t}$ = 5 μm s^{-1}, which is very close to the experimentally observed lipid bilayer front velocity of 3.6 μm s^{-1}. This agreement suggests that close to the channel side, the bilayer formation sharply follows the solvent displacement, *i.e.*, the lipid adsorption kinetics appears to be fast compared to the solvent displacement. Below we test these speculations, by performing a numerical simulation of the full spatiotemporal details of the solvent displacement in the tubes and the channel.

Spatiotemporal evolution. With the reservations given above, we compute the spatiotemporal evolution of the water fraction ϕ in the channel by employing the following advection–diffusion equation

$$\partial_t\phi + \nabla\cdot(\mathbf{u}\phi) = D\nabla^2\phi, \qquad (1)$$

where **u** is the fluid velocity. To numerically integrate this equation, spatial discretization is performed using the first-order upwind scheme for the advection term and the second-order central difference scheme for the diffusion term. Owing to symmetry we simulate only one quarter of the channel. The number of grid points is 100, 8 and 67 in x (stream-wise), y (wall-normal) and z (span-wise) directions, respectively. Grid refinement at the walls is employed, with a grid spacing of $\Delta y = \Delta z$ = 0.05 mm at the walls and increasing with a factor of 1.05 away from the walls. Time integration is performed using the first-order Euler forward scheme. The time step is $\Delta t = \Delta y^2/100D = 5 \times 10^{-4}$ s. The total simulated time is 2000 s, which corresponds to 4×10^6 simulation time steps.

At t = 0 we impose ϕ = 0 throughout the channel. At the walls, we set $\mathbf{n}\cdot\nabla\phi = 0$, where **n** is the wall-normal. This condition, of zero diffusion flux, is also applied at the channel exit ($x = L$) and this treatment is a standard practice in numerical simulations which does not compromise the accuracy of the results sufficiently far away from the outlet.

In order to determine the boundary condition for ϕ at the cannel inlet we conduct additional simulations of the space and time dependencies of ϕ inside the tubing system that connects the buffer reservoir to the channel. The water fraction at the outlet of this system serves as the inlet condition for the channel simulation. To simulate the water fraction in a single tube, we numerically integrate the polar coordinate version of the advection–diffusion eqn (1) with azimuthal invariance,

$$\partial_t\phi + \partial_x(u_x\phi) = D\left(\partial_x{}^2 + \frac{1}{r}\partial_r r\partial_r\right)\phi, \qquad (2)$$

and under fully developed laminar flow conditions, $u_x = Q[1 - (r/R)^2]/(\pi R^2)$, where Q = 0.68 mm^3 s^{-1} is the volumetric flow rate. The inlet condition for the first tube reads as ϕ = 1. The time and radial dependent ϕ-field at the outlet of the first tube is used as the inlet condition for the second tube, and this procedure is repeated for the subsequent tubes. The $\phi(r, t)$ at the outlet of the last (fourth) tube is translated into $\phi(z, t)$ at the channel inlet, by employing the mass conservation principle.

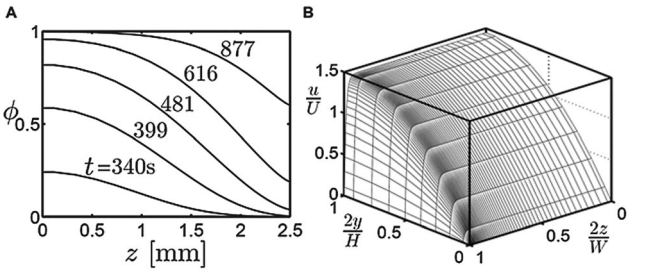

Fig. 5 Details of the solvent displacement simulation. (A) Simulated water fraction ϕ as a function of the span-wise coordinate z and time t at the channel inlet (x = 0). (B) Analytical velocity distribution in the channel cross-section.

The resulting inlet condition for the channel simulation is shown in Fig. 5A.

Turning to the channel simulation, the velocity field **u** that is needed in eqn (1) is not simulated. Instead, we use the analytical expression for the fully developed laminar flow (with constant viscosity) in a rectangular channel,[30] which in the limit of the large aspect ratio (W/H) is reduced to

$$u(y,z) = \frac{3U}{2}\sum_{m=1,3,5,\ldots}\frac{(-1)^{\frac{m-1}{2}}}{m^3}\left(1 - \frac{\cosh\left[\frac{m\pi z}{H}\right]}{\cosh\left[\frac{m\pi}{2}\frac{W}{H}\right]}\right) \times \cos\left[\left(\frac{m\pi}{2}\right)\left(1 - \frac{2y}{H}\right)\right]. \qquad (3)$$

In our simulation we have retained five terms in the series, *i.e.*, m = 1, 3, 5, 7, and 9. The corresponding velocity profile is shown in Fig. 5B for W/H = 50 together with the computational grid in the cross-stream plane. To justify fully developed conditions, we estimate the length, required for the flow to become fully developed, as[31] $UH^2/\nu \approx 10^{-2}$ mm, where U = 1.36 mm s^{-1} is the averaged fluid velocity in the channel, H = 0.1 mm is the channel height and ν = 1 mm^2 s^{-1} is the kinematic viscosity of water. Since this so-called ''entrance length'' is much smaller than the channel length of L = 48 mm, we may assume fully developed conditions throughout the channel. In addition, we may notice that the viscosity (to be specific, we use the viscosity of water) of the isopropanol mixture varies with the water fraction within a three-fold range.[29] For this reason, the real velocity close to the channel side walls is somewhat smaller than that given by eqn (3). In this work, however, we ignore this complication.

Solvent displacement. Typical results of the solvent displacement simulation in the channel are shown in Fig. 6, exhibiting the water-fraction profiles along three directions at various time instances t. As anticipated, the stream-wise distribution $\phi(x, t)$ along the middle of the bottom wall (at y = 0 and z = 0) is nearly uniform (Fig. 6A), due to the fast solvent displacement inside the channel, as compared to the slow displacement and strong mixing inside the tubing system. The wall-normal distribution $\phi(y, t)$ in the channel center ($x = L/2$ and z = 0) is fully uniform due to the fast diffusion kinetics (Fig. 6B). In contrast, the span-wise

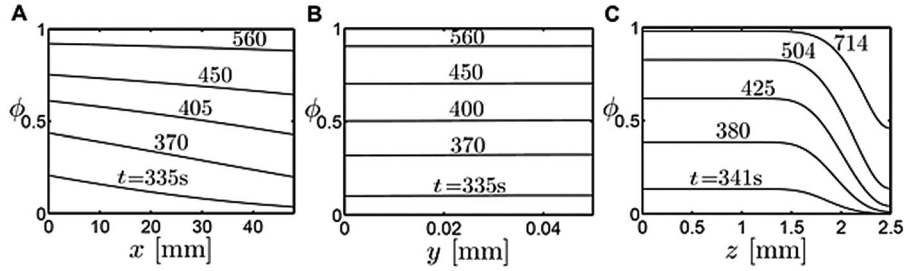

Fig. 6 Simulated spatiotemporal water-fraction profiles. The simulated water fraction profiles in the channel at various time instances t. (A) Water fraction ϕ as a function of the stream-wise coordinate x on the centerline of the bottom wall, $z = 0$ and $y = 0$. The inlet is located at $x = 0$ mm. (B) ϕ as a function of the bottom-wall-normal coordinate y, in the channel center $x = L/2$ and $z = 0$. The bottom wall is located at $y = 0$ mm. (C) ϕ as a function of the span-wise coordinate z, halfway in the channel on the bottom wall, $x = L/2$ and $y = 0$. The side wall is located at $z = 2.5$ mm.

distribution $\phi(z, t)$ at $x = L/2$ and $y = 0$ is uniform in the center of the channel and non-uniform close to the boundaries (Fig. 6C). These profiles show that the solvent exchanges first in the central region and then outwards towards the channel side walls. The observed steepness of the profiles is attributed to slow diffusion kinetics. The uniform stream-wise (Fig. 6A), wall-normal (Fig. 6B) and non-uniform span-wise (Fig. 6C) distributions are in qualitative agreement with order of magnitude estimations, presented above.

Next, we further analyze the span-wise solvent displacement, as shown in Fig. 6C. The observed steep profiles, most notable in the range 1.8 mm $< z <$ 2.2 mm, could be responsible for the experimentally observed lipid bilayer front (see Fig. 3). This hypothesis means that in this particular region, the experimentally determined bilayer formation velocity of 3.6 μm s^{-1} (Fig. 3C) may be directly linked to the solvent displacement. To test this hypothesis, we define the solvent displacement velocity v_D as the time derivative of the solvent displacement position, $z_{\phi^*}(t)$, which in turn is defined as the point along the z-axis (at $x = L/2$ and $y = 0$), where the water fraction (Fig. 6C) equals a threshold value ϕ^*, *i.e.*, $\phi(z_{\phi^*}, t) = \phi^*$. Fig. 7A and B show for various ϕ^*-values, the resulting $z_{\phi^*}(t)$ and $v_D(z_{\phi^*}) = dz_{\phi^*}/dt$, respectively. In the range, 2.2 mm $< z <$ 2.4 mm, which corresponds to the experimental observations (Fig. 3), the simulated displacement velocity (Fig. 7B) is in the range from 1 μm s^{-1} to 4 μm s^{-1}. This range agrees with the experimentally measured bilayer spreading velocity of 3.6 μm s^{-1}.

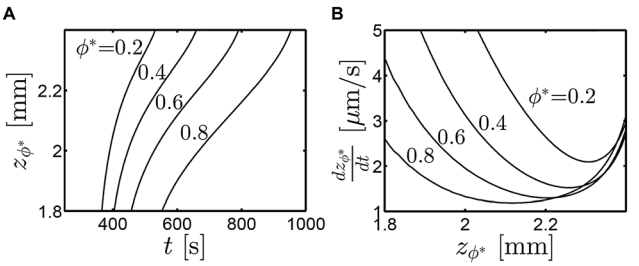

Fig. 7 Simulated solvent displacement velocity. (A) Simulated solvent displacement position z_{ϕ^*} as a function of time t for various values of the threshold water-fraction ϕ^*. (B) Simulated solvent displacement velocity dz_{ϕ^*}/dt as a function of z_{ϕ^*} for various ϕ^*-values.

Discussion

The agreement between the simulated solvent displacement velocity and the experimentally observed bilayer formation velocity suggests that in close proximity to the side walls, the bilayer formation is confined to a relatively thin region behind the moving solvent displacement front. To further strengthen this assertion, we estimate the extent of the bilayer formation region. This quantity is referred to as the bilayer formation length, $\mathcal{L} = v_D\tau$, defined as the product of the solvent displacement velocity v_D, and the so-called bilayer formation time, $\tau = \rho/kc$. Here c is the lipid bulk concentration, ρ is the lipid bilayer mass per area and k is the lipid adsorption rate constant. Under similar conditions to those in the present setup, vesicle adsorption has been shown to be limited by vesicle diffusion in the bulk solution.[32] As SALB formation is believed to be due to the adsorption of micelles and/or vesicles,[21] we assume that in the present setup the SALB formation is also limited by diffusion. Diffusion-limited adsorption corresponds to an adsorption rate constant of $k = D_l/\delta$. Here D_l is the diffusion coefficient of the lipid aggregates and δ is the boundary layer thickness of the lipid bulk concentration field. The diffusion coefficient is estimated with the Stokes–Einstein relation, $D_l = k_BT/(6\pi\eta\xi)$, where ξ is the aggregate radius, k_BT is the Boltzmann energy and η is the dynamic viscosity of the water isopropanol mixture. The laminar boundary layer thickness is estimated as[33,34] $\delta \approx \sqrt[3]{D_l x H/U}$, where U is the channel flow velocity, $x = L/2$ is the flow distance from the channel inlet to the imaging location and H is the channel height. Combining these estimates, we find for the bilayer formation length, $\mathcal{L} \approx 6\frac{v_D\rho}{c}\left(\frac{\eta\xi}{k_BT}\right)^{\frac{2}{3}}\left(\frac{LH}{U}\right)^{\frac{1}{3}}$. Using U = 1.4 mm s^{-1}, L = 48 mm, H = 0.1 mm, v_D = 3 μm s^{-1} (simulation), c = 0.5 μg mm^{-3}, η = 3 g $(ms)^{-1}$,[29] ρ = 4 ng mm^{-2} [22] and ξ = 10 nm for micelles and ξ = 50 nm for vesicles, we estimate $\mathcal{L}$ = 0.08 mm for micelles and $\mathcal{L} = 0.2$ mm for vesicles. These relatively small values of $\mathcal{L}$, as compared to the channel width of W = 5 mm, confirm that the bilayer follows the solvent displacement close to the side walls. In reality, as already noticed, the bilayer formation is expected to occur at a late stage of the solvent-exchange process. Therefore c may be smaller than the

initial value, $c = 0.5\ \mu g\ mm^{-3}$, used in our estimates, although it does not influence the scale of the estimates and conclusions. With increasing temperature in the system, it could be expected that the time scale of the SALB formation process becomes shorter due to the diffusion-limited adsorption behavior. Considering that temperature influences various, often hidden factors in the system,[35] it would be interesting further to explore how temperature influences the spatiotemporal dynamics of the SALB formation process.

Conclusion

In this study, we have used epifluorescence microscopy to experimentally visualize SALB formation involving the deposition of DOPC lipids on a glass surface in a rectangular channel. The interpretation of these observations is supported by a numerical simulation of the solvent displacement in the channel. Special focus has been on the bilayer formation close to the channel side walls. The simulated solvent displacement velocity, a few $\mu m\ s^{-1}$, is found to be in the same range as the measured bilayer spreading velocity towards the wall. Assuming diffusion-limited adsorption kinetics we argue that close to the sidewalls the bilayer forms within a thin region behind the moving solvent displacement front. Finally, we notice that our experimental and theoretical results are obtained for specific values of the flux velocity and the lipid concentration in solution. Upon increasing the flux velocity and/or decreasing the lipid concentration, the SALB formation may become incomplete and may be more sensitive to the lipid adsorption rate.[22] With this reservation, we believe that the key aspects of our measurements and theoretical analysis are generic, and accordingly the results presented may potentially be useful in analyzing various biointerfacial phenomena.

Acknowledgements

We acknowledge support from the National Research Foundation (NRF-NRFF2011-01 and NRF2015NRF-POC0001-19) and Nanyang Technological University to N.J.C. V. P. Zh. is a recipient of the Tan Chin Tuan Exchange Fellowship at Nanyang Technological University.

References

1 E. Sackmann, *Science*, 1996, **271**, 43–48.
2 Y. H. M. Chan and S. G. Boxer, *Curr. Opin. Chem. Biol.*, 2007, **11**, 581–587.
3 G. J. Hardy, R. Nayak and S. Zauscher, *Curr. Opin. Colloid Interface Sci.*, 2013, **18**, 448–458.
4 A. Gunnarsson, A. Snijder, J. Hicks, J. Gunnarsson, F. Höök and S. Geschwindner, *Anal. Chem.*, 2015, **87**, 4100–4103.
5 N. J. Cho, C. W. Frank, B. Kasemo and F. Höök, *Nat. Protoc.*, 2010, **5**, 1096–1106.
6 P. S. Cremer and S. G. Boxer, *J. Phys. Chem. B*, 1999, **103**, 2554–2559.
7 R. Richter, A. Mukhopadhyay and A. Brisson, *Biophys. J.*, 2003, **85**, 3035–3047.
8 D. Axelrod, D. E. Koppel, J. Schlessinger, E. Elson and W. W. Webb, *Biophys. J.*, 1976, **16**, 1055–1069.
9 P. Jönsson, M. P. Jonsson, J. O. Tegenfeldt and F. Höök, *Biophys. J.*, 2008, **95**, 5334–5348.
10 G. H. Zan, J. A. Jackman, S.-O. Kim and N.-J. Cho, *Small*, 2014, **10**, 4828–4832.
11 N. Vila, M. Puggelli and G. Gabrielli, *Colloids Surf., A*, 1996, **119**, 95–104.
12 E. Reimhult, F. Höök and B. Kasemo, *Langmuir*, 2003, **19**, 1681–1691.
13 R. P. Richter and A. R. Brisson, *Biophys. J.*, 2005, **88**, 3422–3433.
14 J. A. Jackman, G. H. Zan, Z. Zhao and N.-J. Cho, *Langmuir*, 2014, **30**, 5368–5372.
15 K. Dimitrievski, *Langmuir*, 2010, **26**, 3008–3011.
16 J. A. Jackman, Z. Zhao, V. P. Zhdanov, C. W. Frank and N.-J. Cho, *Langmuir*, 2014, **30**, 2152–2160.
17 N.-J. Cho, J. A. Jackman, M. Liu and C. W. Frank, *Langmuir*, 2011, **27**, 3739–3748.
18 E. Reimhult, F. Höök and B. Kasemo, *Phys. Rev. E: Stat., Nonlinear, Soft Matter Phys.*, 2002, **66**, 051905.
19 S. Boudard, B. Seantier, C. Breffa, G. Decher and O. Felix, *Thin Solid Films*, 2006, **495**, 246–251.
20 J. A. Jackman, J.-H. Choi, V. P. Zhdanov and N.-J. Cho, *Langmuir*, 2013, **29**, 11375–11384.
21 A. O. Hohner, M. P. C. David and J. O. Rädler, *Biointerphases*, 2010, **5**, 1–8.
22 S. R. Tabaei, J.-H. Choi, G. Haw Zan, V. P. Zhdanov and N.-J. Cho, *Langmuir*, 2014, **30**, 10363–10373.
23 J. A. Jackman, S. R. Tabaei, Z. Zhao, S. Yorulmaz and N.-J. Cho, *ACS Appl. Mater. Interfaces*, 2014, **7**, 959–968.
24 S. R. Tabaei, S. Vafaei and N.-J. Cho, *Phys. Chem. Chem. Phys.*, 2015, **17**, 11546–11552.
25 S. R. Tabaei, J. A. Jackman, B. Liedberg, A. N. Parikh and N.-J. Cho, *J. Am. Chem. Soc.*, 2014, **136**, 16962–16965.
26 S. R. Tabaei, J. A. Jackman, S.-O. Kim, V. P. Zhdanov and N.-J. Cho, *Langmuir*, 2015, **31**, 3125–3134.
27 P. Naira and M. Alam, *Appl. Phys. Lett.*, 2006, **88**, 233120.
28 G. Taylor, *Proc. R. Soc. London, Ser. A*, 1953, **219**, 186–203.
29 K. Pratt and W. Wakeham, *Proc. R. Soc. London, Ser. A*, 1974, **336**, 393–406.
30 D. Holmes and J. Vermeulen, *Chem. Eng. Sci.*, 1968, **23**, 717–722.
31 H. Schlichting, *Boundary-Layer Theory*, McGraw-Hill, 1968.
32 C. A. Keller, K. Glasmästar, V. P. Zhdanov and B. Kasemo, *Phys. Rev. Lett.*, 2000, **84**, 5443–5446.
33 V. G. Levich and S. Technica, *Physicochemical Hydrodynamics*, Prentice-Hall, Englewood Cliffs, NJ, 1962.
34 V. P. Zhdanov, C. A. Keller, K. Glasmästar and B. Kasemo, *J. Chem. Phys.*, 2000, **112**, 900–909.
35 E. Oh, J. A. Jackman, S. Yorulmaz, V. P. Zhdanov, H. Lee and N.-J. Cho, *Langmuir*, 2015, **31**, 771–781.